Electron Temperature Gradient Mode Transport

W. Horton, J.-H. Kim, G. T. Hoang, H. Park, S. M. Kaye, and B. P. LeBlanc

Electron Temperature Gradient Mode Transport

W. Horton and J. -H. Kim

Institute for Fusion Studies, the University of Texas at Austin

G. T. Hoang

Association Euratom-CEA, CEA/DSM.DRFC

H. Park, S. M. Kaye, B. P. LeBlanc

Princeton Plasma Physics Laboratory, Princeton University

(Dated: December 5, 2007)

Anomalous electron thermal losses plays a central role in the history of the controlled fusion program being the first and most persistent form of anomalous transport across all toroidal magnetic confinement devices. In the past decade the fusion program has made analysis and simulations of electron transport a high priority with the result of a clearer understanding of the phenomenon, yet still incomplete. Electron thermal transport driven by the electron temperature gradient is examined in detail from theory, simulation and power balance studies in tokamaks with strong auxiliary heating.

PROPERTIES OF ELECTRON TRANSPORT

Electron temperature profiles respond differently than the density and ion temperature profiles to the influence of externally applied heating and particle sources. In the first toroidal experiments such as the model C-stellarator[1] and the first tokamak[2], it became clear that electron thermal transport could be characterized by an electron thermal diffusivity $\chi_e(\,\mathrm{m^2/s})$ that was much higher than the value that given by collisional transport theory. Theses early devices showed a χ_e that roughly followed the diffusion rate given by Bohm [3], $D_B = \alpha_B(T_e/eB)$ with various values of the numerical coefficient α_B. In the model C-stellarator, for example, α_B was typically 1/50 and in some lower temperature toroidal octopole experiment [4] records were reached with $\alpha = 1/100$ to 1/1000. The scaling T_e/B of the diffusivity seemed secure.

In 1967 Artsimovich went to the Princeton Plasma Physics Laboratory to announce the breakthrough of reaching a record Lawson product of $n_e\tau_E$ at the Kurchatov Laboratory with the T-3 tokamak. Record confinement time of $\tau \simeq 20\,\mathrm{ms}$ were reached in the new T-3 tokamak at Kurchatov. Princeton quickly rebuilt their stellarator into an axisymmetric tokamak using the same ohmic heating transformer system and magnetic field power supplies. The new device, called the

Princeton Large Torus (PLT), reproduced the record energy confinement times $\tau_E \simeq 100\,\text{ms}$ and went on to achieve record ion temperature after $2\,\text{MW}$ of neutral beam heating NBI were added. The electron thermal transport still followed something close to the reduced ($\alpha_B \ll 1/16$) Bohm scaling with a numerical coefficient in the range of $\alpha_B \simeq 10^{-3}$.

Direct measurement of the source of the anomalous plasma transport due to the plasma fluctuations [5] requires very careful determination of the relative phase of density δn and potential $\delta\phi$ fluctuations, since to zeroth order they are in phase, implying no next transport. Measurements of the plasma decay time using a microwave interferometer, Langmuir probes and a total radial loss detector show that the plasma lifetime was roughly 10 times the Bohm diffusion time. The plasma lifetime was measured by the density decay rate after turning off the external drives. Thus the experiments were characterized by $\alpha_B \sim 1/160$ rather than the coefficient of $(1/16)(T_e/eB)$ in diffusion equation for the plasma density.

Modern tokamak experiments routinely have core heating power densities at or above of $P_e/V = 1\,\text{MW/m}^3$ into the electrons. At a density of $5 \times 10^{19}\,\text{m}^{-3}$ this corresponds to an energization rate of $P_e/n_e = 300\,\text{KeV/s}$ giving $\delta T_e = 3\,\text{KeV}$ in $10\,\text{ms}$ of heating in the absence of losses. Typically the electron temperature will saturate from radial thermal transport to the edge plasma where the total heating power P_e is carried away by the limiters and/or the scrape-off-layer plasma. The standard model for the radial thermal loss is a hear flux $q_e = -n_e\chi_e(\mathrm{d}T_e/\mathrm{d}r)$ with typical modern tokamaks having $\chi_e \sim 5 - 50\,\text{m}^2/\text{s}$.

For example, extensive electron transport scaling data is reported by Tore Supra experiments from scans in the externally applied heating power P_e from $0.75\,\text{MW}$ to $7.5\,\text{MW}$ as shown in Fig. 1. The corresponding electron temperature profiles are shown in Fig. 1a and the density n_e and the safety factor q profile in Fig. 1b. The steady state power balance condition then leads to the electron thermal flux $q_e\left[\text{MW/m}^2\right]$ shown in Fig. 1c in the top (red) curves. The lower (black curves) in Fig. 1c show how much heat flux is accounted for by the radiation losses and the transfer of electron energy to lower temperature ions by electron-ion collisions. We see that more than 90% of the electron thermal loss in this set of 8 Tore Supra discharges is carried away by the anomalous or turbulent electron thermal diffusivity.

The Tore Supra data in Fig. 1 is from a classical circular cross section tokamak with $R/a = 2.4\,\text{m}/0.8\,\text{m}$ and a toroidally symmetric pump limiter. The maximum Ohmic heating occurs for the lowest temperature discharge and is approximately $0.75\,\text{MW}$. The data in Fig. 1 has RF heating up to $7.4\,\text{MW}$. More recent experiments have extended the data up to $15\,\text{MW}$ heating with core T_e reaching $9\,\text{KeV}$.
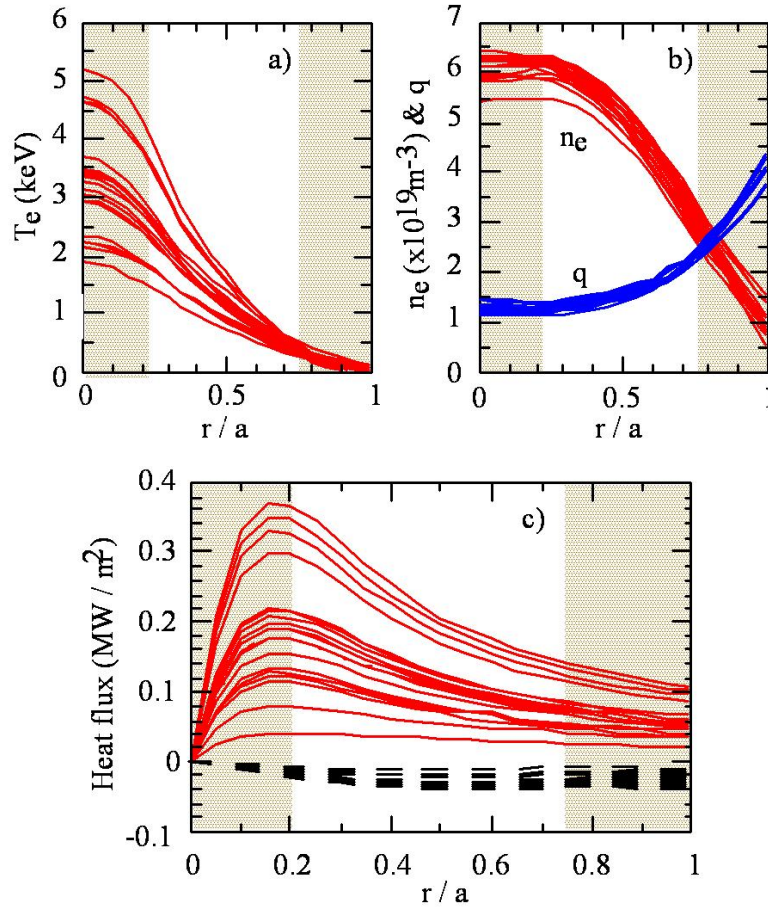
FIG. 1: Profiles of (a) The electron temperature T_e, (b) electron density n_e and safety factor q, and (c) heat fluxes (solid = FW coupled to electrons + Ohmic; dashed = radiation and electron-ion losses) in Tore Supra, $I_p = 0.6\,\mathrm{MA}$, $B = 2.2\,\mathrm{T}$ and $P_{\mathrm{tot}} = 1.5 - 7.5\,\mathrm{MW}$ ($P_{\mathrm{OH}} = 0.1 - 0.75\,\mathrm{MW}$ and $P_{\mathrm{FW}} = 0.75 - 7.4\,\mathrm{MW}$)[6]

The non-resonant fast wave in the ion cyclotron frequency range heats the thermal velocity part of the electron velocity distribution through electron Landau resonances with $\omega_{\mathrm{RF}} = k_{\parallel}^{\mathrm{RF}} v_{\parallel}$ Fast Wave heating. It is the RF heating mechanism favored by Stix [7] for reactors and is used extensively in both Tore Supra and the National Spherical Tokamak Experiment NSTX at PPPL. Compared with higher frequency Lower Hybrid heating and Electron Cyclotron heating, Fast Wave heating gives the least distortion from electron Maxwellian distribution and in this sense is closer to the Ohmic heating mechanism which is known to give the best confinement time properties of the electrons. The problem with Ohmic heating is that the electron heating mechanism becomes very weak at the electron temperatures required for fusion plasmas $T_e > 10\,\mathrm{KeV}$.

.

Fig. 2 shows a typical Fast Wave heating experiment from NSTX where the electron temperature
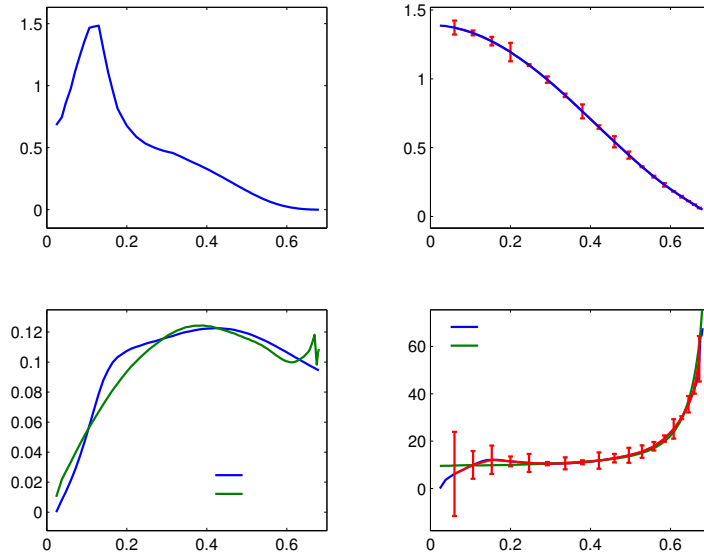
FIG. 2: NSTX profiles and power balance analysis for discharge 106194. From (a) is the electron absorbed RF power density, (b) the 20 cord 17ms Thomson scattering electron temperature profile with a 3% random error added to estimate the uncertainty in the electron power balance analysis, (c) the electron thermal fluxes, q_e from power balance (PB) and from the ETG model and (d) the respective thermal diffusivities with the error estimate for the power balance diffusivity.[8]

profile is measured with high resolution by a combination of high tech instruments. Fig. 2a shows the profile of the core deposited High Harmonic Fast Wave (HHFW) heating, Fig. 2b shows the corresponding electron temperature profile with estimates of the uncertainty from the red arrow bars, Fig. 2c the inferred electron thermal heat flux and compared with a theoretical model called the ETG model and discussed in Sec.. Finally, dividing the electron thermal flux by the electron temperature gradient yields in Fig. 2d the electron thermal diffusivity χ_e. The profile of a low χ_e in core and increasing rapidly toward the edge is a widely observed characteristic of toroidally confined plasmas and can be difficult to reconcile with the theoretical formulas for the anomalous diffusivity.

The resolution of the self consistency problem of the χ_e profiles with the theoretical formulas often requires using the theory formulas in the predictive-interpretative mode of an integrated transport model. These integrated transport models contain sufficient coupling between the multiple channels of power deposition, power flow and power loss to evaluate the performance of the theoretical formulas. Integrated transport codes for this purpose include the BALDUR code of the Lehigh University group, the TRANSP code at PPPL, the CRONOS code at Cadarache and the ASTRA code. An example of the evolution of the electron temperature profile with the ETG
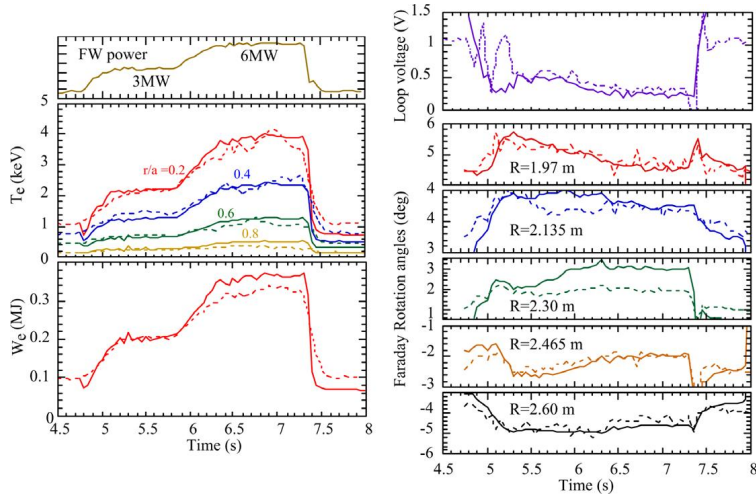
FIG. 3: Tore Supra FWEH discharge #18368 data (dashed curve) compared with the ETG model (solid curve). Top right panel shows the modeled loop voltage (solid) versus the measured voltage (dashed). Lower right panels give the poloidal magnetic field measured (dashed) and predicted (solid) from the Faraday Rotation diagnostics and simulation at four vertical cords.

model corresponding to the χ_e shown in Fig. 2d is shown in Fig. 3 using the CRONOS code in this predictive-interpretative mode in which data values for T_i and edge T_e parameters are used along with a comprehensive ray tracing code for the FW heating power deposition [9].

The electron thermal flux $q_e(r)$ is computed from power balance in the steady state by

$$\frac{1}{r}\frac{\partial}{\partial r}(rq_e) = P_e(r) - Q_{ei}(r) \tag{1}$$

where the electron thermal losses to the colder ions is given by

$$Q_{ei} = 3\frac{m_e}{m_i}\nu_{ei}n_e(T_e - T_i) \tag{2}$$

The electron thermal diffusivity from power balance is computed from

$$\chi_e = -\frac{q_e}{n_e\frac{\partial T_e}{\partial r}} . \tag{3}$$

The ETG has also been successfully used in comparing χ_e from modulated electron cyclotron heated (ECH) plasmas in the Frascati Tokamak named FTU. By modulating the envelop of the ECH power $P_{\mathrm{ECH}}(r,t)$ and measuring the corresponding variations in the temperature profile is one useful way to measure the thermal diffusivity $\chi_e(r)$. In Fig. 4 we show the results of this experiment reported by Jacchia et al. [10] for three different discharges. The results are explained adequately by the ETG model. Jacchia et al. [10] also compare the thermal diffusivity derived from steady state power balance with that obtained by applying heat pulses as shown in Fig. 5 where
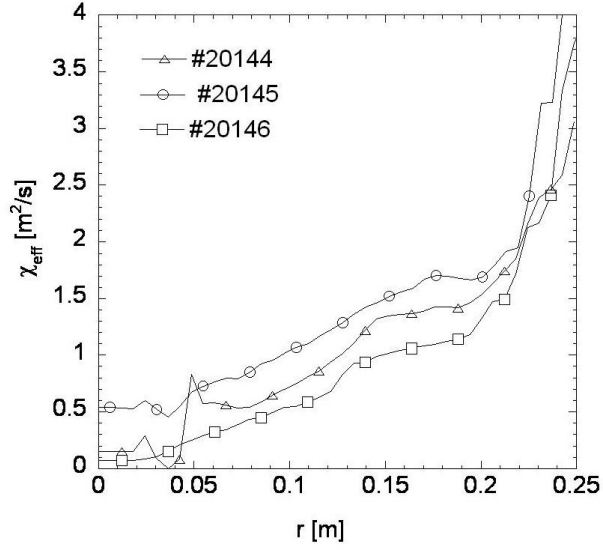
FIG. 4: FTU thermal transport coefficient χ_{eff} as given by the power balance analysis is shown vs radial position r.
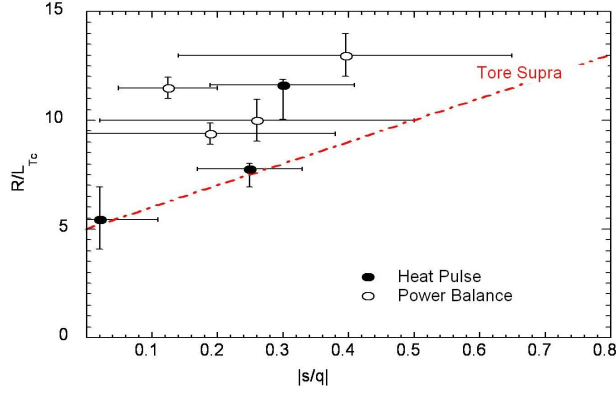

FIG. 5: Dimensionless parameter, R/L_{T_c} from FTU tokamak perturbative and power balance (open symbols) is shown vs the ratio s/q. The offset linear fit of Tore Supra [6] data $(R/L_{T_c} = 5 + 10s/q)$ is also shown in the same figure for the sake of reference $(- \cdot -)$. Error bars on data from perturbative analysis are obtained by propagating the uncertainty in the radial position of the step in χ_{HP} on the determination of $1/L_{Tc}$ and s/q.

the results are expressed in terms of the critical temperature gradient L_{Tc}/R versus the magnetic shear parameter s/q with the Tore Supra thermal balance analysis $(- \cdot -)$. The ETG model also explains the key thermal transport properties of the electron cyclotron heated high T_e plasmas in the TCV tokamak [11].

Similar results are being observed by Asp et al. [11] for the very high power density electron cyclotron wave heating, reaching $6\,\text{MW/m}^3$ at the core of the TCV machine at Lausanne. Heat
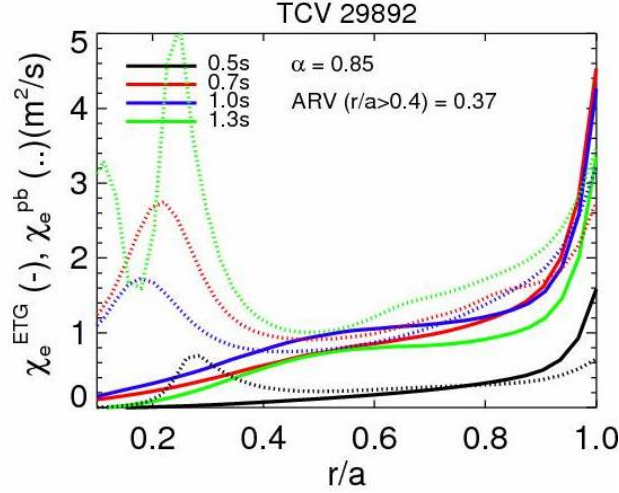
304

FIG. 6: The comparison between the electron gyro-Bohm heat diffusivity, χ_e^{ETG} based on the mixing length argument, (solid) with ETG time and spatial scales and the power balance heat diffusivity χ_e^{pb} (dotted) for each time slice $t = 0.5$(black), 0.7(red), 1.0(blue) and 1.3(green) in TCV 29892.

diffusivities χ_e^{ETG} based on the mixing length theory for ETG with length scale of electron gyro-radius ρ_e and time scale of the electron temperature gradient length divided by electron thermal velocity L_{T_e}/v_{T_e} is shown to be consistent with the power balance diffusivities χ_e^{pb} in the different phases of H-mode, above $r/a > 0.4$. Fig. 6 shows th model and power balance electron thermal diffusivities for the high P_e TCV discharge. The peak of heat diffusivities inside $r/a < 0.4$ shown in Fig. 6 are due to the MHD activity since $q_0 < 1$ and correlate with 3/2-neoclassical tearing mode islands.

We conclude that the ETG model is working for all four machines (TS, NSTX, TCV and FTU) and with different methods of determining the thermal diffusivity. Thus, the ETG model has been verified as an important theoretical model for explaining the anomalous electron thermal transport in toroidal systems.

Now, we turn to explaining the theoretical structure of the ETG model.

PHYSICAL MECHANISM OF THE ETG TURBULENT TRANSPORT

For drift wave turbulence from the space scales of the electron gyro-radius down to the ion gyro-radius, the effect of the local maximum and minimum of the electrostatic potentials is as shown in Fig. 7. At this scale length only the electrons are able to $\boldsymbol{E} \times \boldsymbol{B}$ drift and follow, with their guiding centers, the isopotential contour shown in Fig. 7 as circle. The ion gyro-radius is so large compared with the scale of the fluctuation that the electric field is averaged over the ion orbit to a

ETG Drift Waves

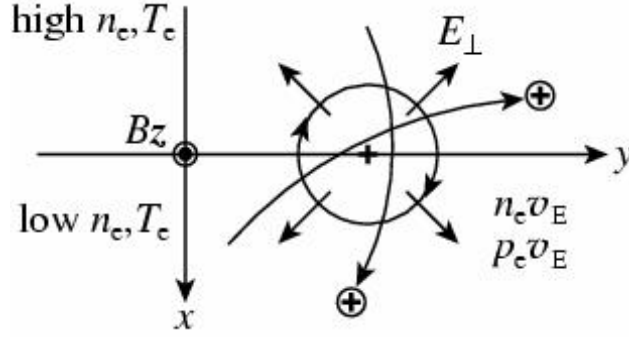
FIG. 7: Scheme of drit waves at the electron gyro-radius scale

small value. There only remains the local Boltzmann response of the ion density $\delta n_i = -n_i e\phi/T_i$ to first approximation in the wavelength $\lambda_\perp/\rho_i < 1$. Later on we can insert perturbatively the effect of small, resonant ion contributions from high energy ions that can resonate ($\omega_{\boldsymbol{k}}^{\mathrm{ETG}}$ with the high ETG wave frequency $\omega = k_y \rho_e v_e/L_{Te} \sim 0.3 v_e/L_{Te} \gg c_s/L_n$).

Owing to this high frequency-short scale length of the ETG modes the electrons that resonate with the waves are the thermal electrons rather than the low energy electrons as in the usual drift waves. The ETG mode does not depend on the electrons being magnetically trapped as in the trapped electron mode in Chap. 1. The mode is driven by the electron temperature gradient $\boldsymbol{\nabla} T_e$ and has both a slab version with an effective adiabatic gas constant of $\Gamma = 3$ and threshold $\eta_e = 2$ and a toroidal version with $\Gamma = 5/3$ and $\eta_e = 2/3$ for the case of weak magnetic shear and $k_y \rho_e < 1$.

These threshold formulas for the critical electron temperature-to-density gradient follow from the Nyquist analysis of the Vlasov-Poisson dispersion relation. The results are easily understood from the Carnot cycle analysis introduced in Chap. 1. We repeat the physical picture since it is important for understanding why the plasma collective modes in the ETG regime create long, extended radial structures with $\ell_c \gg \rho_e$ called "streamers". The increase of the released thermal-gradient energy by the turbulence with ℓ_c^2 follow from the maximum energy released by the Carnot engine operating between T_1 and T_2 separated by the correlation length ℓ_c shown in Fig. 3 of Chap. 1. The thermodynamic calculation requires the value of the effect gas constant Γ and the temperature-to-density gradient ratio $\eta_e = d\ln T_e/d\ln n_e$. The result gives the maximum energy that the spontaneous plasma convection can release in to the ETG mode and thus provides the useful upper bound on the ETG turbulence level. This released energy density W_{ETG} is a very small fraction the thermal energy density $3/2 n_e T_e$ of the electron component of the plasma. However,

the power transfer $2\gamma W$ from the plasma to the waves of energy density W is high due to the growth rate of the instability being in the range of $\gamma \sim 0.3 v_e/(L_{Te}R)^{1/2} > 10^6\,\mathrm{s}^{-1}$.

GYROFLUID ETG MODEL

The basic electron temperature gradient turbulence may be described with three partial differential equations for the fluctuating electrostatic potential $\phi(\boldsymbol{x},t)$, the fluctuating parallel vector potential $A_\parallel(\boldsymbol{x},t)$ and the electron temperature $\delta T_e(\boldsymbol{x},t)$ fluctuation. These are finite electron gyro-radius fluid equations that are valid in the wavenumber range $\rho_i^{-1} \leq k_\perp \leq \rho_e^{-1}$ where ρ_i is the ion gyro-radius and ρ_e is the electron gyro-radius. The fluid description parallel to $\boldsymbol{B}$ uses a closure for the chain form p_e to $\nabla_\parallel q_{e\parallel}$ to describe accurately the parallel electron Landau resonances $\tilde{\omega} = \omega - \omega_E - \omega_{De} = k_\parallel v_\parallel$ and the trapped electron response. The parallel electron heat flux $q_\parallel(\boldsymbol{k})$ is closed [12, 13] either in the adiabatic limit described by the adiabatic gas constant Γ or with Landau-fluid closure which is strongly dissipative with $\tilde{q}_\parallel(\boldsymbol{k}) = \chi_{e\parallel}|k_\parallel|v_e n_e \delta T_e(\boldsymbol{k})$, where $\chi_{e\parallel}$ is a suitable constant of order unity. Typically $\chi_{e\parallel}$ is chosen to match the associated growth rate $\gamma(\boldsymbol{k}_\perp, k_\parallel, \chi_{e\parallel})$ with the values derived from the kinetic dispersion relation that is free of the closure problem.

The ETG instability is robust once the critical gradient $(\eta_e > \Gamma - 1 + L_n/L_s(1 + T_e/T_i))$ is exceeded. Thus, the lack of a precise wave-particle resonances dissipation fluid closure does not cause a serious limit on the validity of the turbulence model. The advantage of the FLR-fluid description is that with the pseudo-spectral computer algorithm and large grid sizes (512×512, $0.025 < k_y\rho_e < 2.5$) run within a few hours of CPU time. Advanced gyrokinetic simulations [14, 15] confirm that large boxes with small $k_y\rho_e$ values are required to give converged values of $\chi_e t$.

The dominant feature of the nonlinear simulations is a strong inverse cascade to large perpendicular wavelengths that yield large enhancement (factors of 10-70) over the ETG weak turbulence mixing length formula $\gamma_k/k_\perp^2$ for the diffusivity. In the base-line core simulation for the NSTX 120967, we obtain a numerical coefficient of order 10-20 for the numerical factor in the gyro-Bohm formula. Fig. 8 shows the growth and saturation of the ETG turbulence spectrum for a mid-radius point in the NSTX discharge 120967. The figure shows clearly the exponential growth of modes at $k_y\rho_e \sim 0.3$ in the early stage and the nonlinear transfer to the low $k\rho_e \leq 0.1$ in the final nonlinear stage.

That the inverse cascade gives rise to the large enhancements of χ_e over the electron gyro-Bohm $\chi_e^{gB} = \rho_e v_e^2/L_{Te}$ value are reported in the many works (Nevins et al. [15], Li and Kishimoto
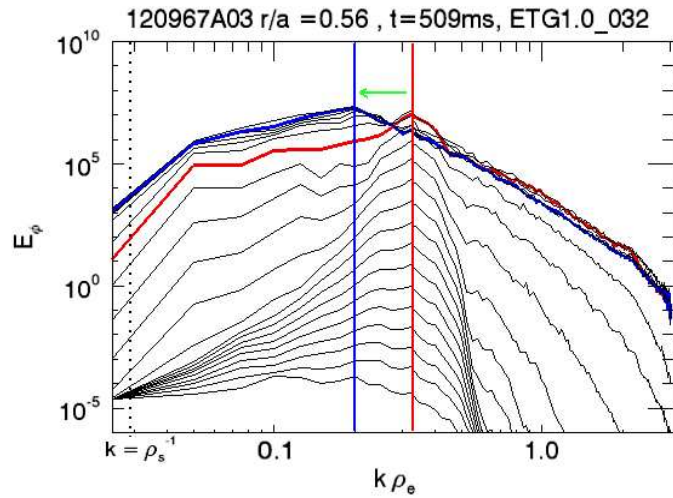
FIG. 8: Gyrofluid k-spectrum of perturbed electrostatic potential at $r/a = 0.56$ and $t = 509\,\mathrm{ms}$ for NSTX 120967 with parameters $\eta_e = -2.72$, $\epsilon_n = -0.858$ and $T_e = T_i$

[16, 17], Holland and Diamond [18]) and are due to extended radial coherent structures. The thermal flux $q_e(t)$ is typically intermittent as the large space scale coherent structures form and dissolve.

Both the gyrokinetic and the FLR-fluid simulation codes see structures with correlation lengths $l_x \leq 100\rho_e$ and $l_y \leq 30\rho_e$ that are intermittent in space and time as shown in Fig. 9 from the five-dimensional continuum GKV code [19]. To find a saturated nonlinear state requires a larger simulation box than for the corresponding ITG simulations. Watanabe used a box with $L_x = 292\rho_e$ and $L_y = 190\rho_e$ in Fig. 9. The transport in the saturated nonlinear state has $\langle \chi_e \rangle \simeq 20\chi_e^{gB}$ for $\eta_e = 3$, $s/q = 0.57$ and $T_e = T_i$.

The large radially extended coherent structures shown in Fig. 9 from the 5D GKV Watanabe code are similar to those seen in the FLR-Landau fluid simulation and produce the large enhancement of χ_e over the gyro-Bohm value.

Now we summarize the use of the electromagnetic fluid ETG turbulence simulation together with the theory to interpret the χ_e^{PB} in NSTX [20].

The electromagnetic ETG equation contains the electron scale c/ω_{pe} microtearing modes [21] through the nonlinear interaction of ϕ, $A_\parallel$ and $\nabla^2 A_\parallel$. When there is an electron temperature fluctuation δT_e, the electron tearing mode transforms to the electron drift-tearing mode with the magnetic reconnection (MRC) component $\delta B_x = ik_y A_\parallel$. The parallel electron streaming along
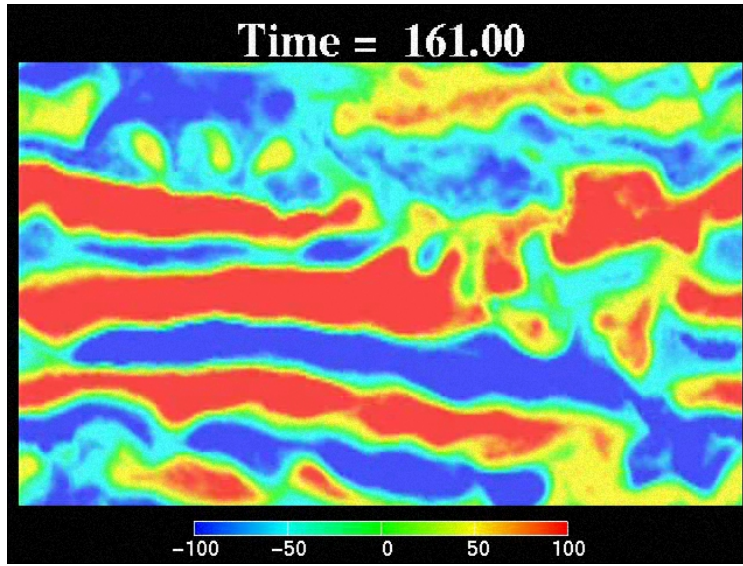
FIG. 9: Streamer formation in the ETG gyrokinetic-Vlasov GKV code simulation (T. Watanabe). The box size is $(L_x, L_y) = (292, 190)\rho_e$ and the magnetic shear $s =?$ and $q =?$.

$\delta \boldsymbol{B}$ gives an additional thermal flux. The main flux q_x^e remains from $\boldsymbol{E} \times \boldsymbol{B}$ convection given by $2\epsilon_n q_x^e$ where $q_x^e = n \langle \delta T_e \tilde{v}_x \rangle$ in the electron thermal flux. The nonlinear transfer between the MRC energy and the electron thermal energy occurs with the conservative coupling terms $-\delta J_\parallel \nabla_\parallel \delta p_e$ and $\delta p_e \nabla_\parallel \delta J_\parallel$ in the parallel acceleration equation and in the electron thermal equation.

Basic structure of the ETG model given in Horton et al. [8], Holland and Diamond [18] and Li and Kishimoto [16, 17] is

$$\hat{\boldsymbol{T}}\boldsymbol{\Phi} + \hat{\boldsymbol{L}}\boldsymbol{\Phi} = \hat{\boldsymbol{N}}(\boldsymbol{\Phi}, \boldsymbol{\Phi}) \tag{4}$$

where $\boldsymbol{\Phi} = (\phi, A_\parallel, T_e)$ is the field vector and $\hat{\boldsymbol{T}}$ are the first order time derivatives and $\hat{\boldsymbol{L}}$ and $\hat{\boldsymbol{N}}$ are linear and nonlinear spatial differential operators, respectively.

The operators in Eq. (4) are

$$
\begin{aligned}
\hat{\boldsymbol{T}}_{11} &= (-1 + \nabla_\perp^2)\frac{\partial}{\partial t} \\
\hat{\boldsymbol{T}}_{22} &= \left(-\frac{\beta}{2} + \nabla_\perp^2\right)\frac{\partial}{\partial t} \\
\hat{\boldsymbol{T}}_{33} &= \frac{\partial}{\partial t} \\
\hat{\boldsymbol{T}}_{ij} &= 0 \quad \text{where} \quad i \neq j
\end{aligned}
$$

$$\hat{\boldsymbol{L}}_{11} = (1 - 2\epsilon_n + (1+\eta_e)\nabla_\perp^2)\tfrac{\partial}{\partial y}) - \mu\nabla^4, \quad \hat{\boldsymbol{L}}_{12} = \nabla_\perp^2 \tfrac{\partial}{\partial z}, \qquad\qquad \hat{\boldsymbol{L}}_{13} = 2\epsilon_n \tfrac{\partial}{\partial y}$$

$$\hat{\boldsymbol{L}}_{21} = -\tfrac{\partial}{\partial z}, \qquad\qquad \hat{\boldsymbol{L}}_{22} = -\tfrac{\beta}{2}(1+\eta_e)\tfrac{\partial}{\partial y} + \tfrac{\eta}{\mu}\nabla_\perp^2, \quad \hat{\boldsymbol{L}}_{23} = \tfrac{\partial}{\partial z}$$

$$\hat{\boldsymbol{L}}_{31} = (\eta_e - 4\epsilon_n(\Gamma - 1))\tfrac{\partial}{\partial y}, \qquad \hat{\boldsymbol{L}}_{32} = (\Gamma - 1)\nabla_\perp^2 \tfrac{\partial}{\partial z},$$

$$\hat{\boldsymbol{L}}_{33} = 2\epsilon_n(\Gamma - 1)\tfrac{\partial}{\partial y} - \chi_\perp \nabla_\perp^2 - \chi_\| \tfrac{\partial^2}{\partial z^2}$$

$$\hat{\boldsymbol{N}}_1 = \hat{\boldsymbol{N}}_{111} + \hat{\boldsymbol{N}}_{122} = - \left[\phi, \nabla_\perp^2 \phi\right] + \frac{\beta}{2}\left[A_\|, \nabla_\perp^2 A_\|\right]$$

$$\hat{\boldsymbol{N}}_2 = \hat{\boldsymbol{N}}_{212} + \hat{\boldsymbol{N}}_{221} + \hat{\boldsymbol{N}}_{223} = - \left[\phi, \nabla_\perp^2 A_\|\right] - \frac{\beta}{2}\left[A_\|, \phi - T_e\right]$$

$$\hat{\boldsymbol{N}}_3 = \hat{\boldsymbol{N}}_{313} + \hat{\boldsymbol{N}}_{322} = - \left[\phi, T_e\right] + (\Gamma - 1)\frac{\beta}{2}\left[A_\|, \nabla_\perp^2 A_\|\right]$$

where $[f, g] = \partial_x f \partial_y g - \partial_y f \partial_x g$ is the Poisson bracket arising from $\boldsymbol{v}_E \cdot \boldsymbol{\nabla}$ convection and $\delta \boldsymbol{B} \cdot \boldsymbol{\nabla}$ line bending. In deriving energy conservation the conservation properties for the double periodic boundary condition,

$$< f\,[f, g] > = \int f\,[f, g]\, d\boldsymbol{x} = 0$$

$$< f[g, h] > = < g[h, f] > = < h[f, g] >$$

$$< f[g, h] > = - < g[f, h] > = - < h[g, f] >$$

are used. The double periodic boundary conditions eliminates the surface effects as in condensed matter physics.

The three energy component equations become

$$\frac{\partial W_E}{\partial t} = < \phi \hat{\boldsymbol{L}}_{11}\phi > + < \phi \hat{\boldsymbol{L}}_{12} A_\| > + < \phi \hat{\boldsymbol{L}}_{13} T_e > - < \phi \hat{\boldsymbol{N}}_{122} >$$

$$= - \left\langle \mu |\boldsymbol{\nabla}_\perp \phi|^2 \right\rangle + \left\langle \phi \nabla_\perp^2 \frac{\partial A_\|}{\partial z} \right\rangle + 2\epsilon_n \left\langle \phi \frac{\partial T_e}{\partial y} \right\rangle - \frac{\beta}{2}\left\langle \phi\,[A_\|, \nabla_\perp^2 A_\|] \right\rangle$$

$$\frac{\partial W_B}{\partial t} = - < \nabla_\perp^2 A_\| \hat{\boldsymbol{L}}_{21}\phi > - \left\langle \nabla_\perp^2 A_\| \hat{\boldsymbol{L}}_{22} A_\| \right\rangle - < \nabla_\perp^2 A_\| \hat{\boldsymbol{L}}_{23} T_e > + < \nabla_\perp^2 A_\| (\hat{\boldsymbol{N}}_{221} + \hat{\boldsymbol{N}}_{223}) >$$

$$= - \left\langle \phi \nabla_\perp^2 \frac{\partial A_\|}{\partial z} \right\rangle - \frac{\eta}{\mu_0}\left\langle |\nabla_\perp^2 A_\||\right\rangle + \left\langle T_e \nabla_\perp^2 \frac{\partial A_\|}{\partial z} \right\rangle + \frac{\beta}{2}\left\langle \phi\,[A_\|, \nabla^2 A_\|] \right\rangle - \frac{\beta}{2}\left\langle T_e\,[A_\|, \nabla^2 A_\|] \right\rangle$$

$$\frac{\partial W_{T_e}}{\partial t} = \frac{1}{\Gamma - 1}\left(- < T_e \hat{\boldsymbol{L}}_{31}\phi > - < T_e \hat{\boldsymbol{L}}_{32} A_\| > - < T_e \hat{\boldsymbol{L}}_{33} T_e > + < T_e \hat{\boldsymbol{N}}_{322} > \right)$$

$$= \left(\frac{\eta_e}{\Gamma - 1} - 4\epsilon_n \right)\left\langle \phi \frac{\partial T_e}{\partial y} \right\rangle - \left\langle T_e \nabla_\perp^2 \frac{\partial A_\|}{\partial z} \right\rangle - \left\langle \chi_\perp |\boldsymbol{\nabla}_\perp T_e|^2 + \chi_\| \left| \frac{\partial T_e}{\partial z} \right|^2 \right\rangle + \frac{\beta}{2}\left\langle T_e\,[A_\|, \nabla_\perp^2 A_\|] \right\rangle$$

where

$$W_E = \frac{1}{2}\left\langle \tau |\phi|^2 + |\boldsymbol{\nabla}_\perp \phi|^2 \right\rangle$$

$$W_B = \frac{1}{2}\left\langle \frac{\beta}{2}|\boldsymbol{\nabla}_\perp A_\||^2 + |\nabla_\perp^2 A_\||^2 \right\rangle$$

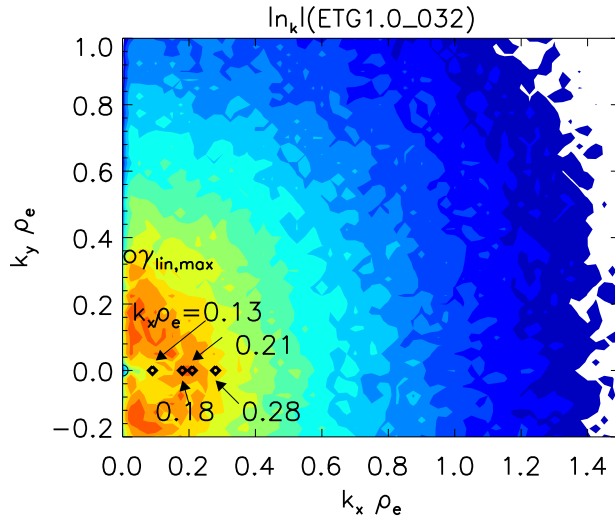$$W_{T_e} = \frac{1}{2(\Gamma - 1)}\left\langle |T_e|^2 \right\rangle$$

FIG. 10: Spectral distribution in saturated state of ETG simulation NSTX showing with diamonds the location of the measured $|\delta n_e(\boldsymbol{k})|$

The total energy evolves with

$$
\frac{\partial}{\partial t}\left(W_E + W_B + W_{T_e}\right) = \left(\frac{\eta_e}{\Gamma - 1} - 2\epsilon_n\right)\left\langle\phi\frac{\partial T_e}{\partial y}\right\rangle
$$

$$
- \mu\left\langle|\nabla_\perp^2\phi|^2\right\rangle - \frac{\eta}{\mu_0}\left\langle|\nabla_\perp^2 A_\parallel|^2\right\rangle - \chi_\perp\left\langle|\boldsymbol{\nabla}_\perp T_e|^2\right\rangle - \chi_\parallel\left\langle\left|\frac{\partial T_e}{\partial z}\right|^2\right\rangle \quad (5)
$$

In the saturated time-averaged steady state the time average of the RHS of Eq. (5) vanishes. Thus the sum of the four dissipation terms $(\mu, \eta/\mu_0, \chi_\perp, \chi_\parallel)$ balances the temperature gradient minus the critical gradient times the heat flux $q_e = \langle\phi\partial T_e/\partial y\rangle = -\langle E_y\delta T_e\rangle/B/$ which drives the turbulence in the first term on the RHS of Eq. (5) and in $\boldsymbol{k}$-space is

$$
q_e = \sum_{\boldsymbol{k}}\frac{[\operatorname{Im} k_y\phi^*(\boldsymbol{k})\delta T_e(\boldsymbol{k})]}{B}. \quad (6)
$$

VERIFICATION OF THE ETG MODEL WITH TOKAMAK DATA

A distinguishing characteristic of the ETG model is that the bulk of the electrons distribution function oscillates with the wave frequency so that there is a significant oscillating parallel electric current $\delta j_\parallel$. The resulting magnetic field δB_x while typically too small to add appreciably to the $\langle v_{\boldsymbol{E}\times\boldsymbol{B},x}\delta p_e\rangle$ thermal heat flux is a distinguishing feature of the mode. The internal magnetic fluctuations, however, were measured in Tore Supra with the cross-polarization scattering technique in which the incident extraordinary electromagnetic wave (X mode) is scattered by the nonlinear

Lorentz force from the δB_x fluctuation of the plasma into the outgoing ordinary electromagnetic mode (O mode). This diagnostic was developed in detail in the Tore Supra group by Zou et al. [22] and Colas et al. [23] from a proposal by Gressilon, and while not without some issues,the experiment confirms the presence of a spectrum of δB_x fluctuations at the level predicted by the ETG theory. The Colas et al. [23] experiments report that there is a correlation between the increasing intensity of these magnetic fluctuations with increasing levels of electron thermal flux q_e and the increasing electron temperature gradient $\boldsymbol{\nabla} T_e$. These are the key features of the ETG model, thus contributing the verification of the model.

Reflectometer measurements of the fluctuating electron density down to the ρ_e scale lengths have been reported by Kaye et al. [20]. The measurements and the correlation with turbulence theory modeling are shown in Fig. 10. While one sees from Fig. 10 that the part of the spectrum with largest amplitude (red) and the largest contribution to the thermal flux is not directly measured, theory gives a fixed relation between the maximum flux components and the measured $|n_{\boldsymbol{k}}|$ components of the spectrum. The new data showing significant reflected (backscattered) electromagnetic wave from the small scale electron density turbulence is found to be as predicted by the ETG model.

This area of research of the micron to millimeter scale range of plasma turbulence is an exciting new area recommended to incoming researchers in both experimental and simulations analysis of confined plasmas. The potential rewards to the search for fusion power from understanding better and controlling the turbulent electron transport is indeed great.

The record confinement shots toward achieving the highest fusion triple product and thus the highest value of the fusion power amplification factor Q_f are found in tokamaks where an internal electron thermal transport barrier has been created. While still a hot topic of research the electron internal transport barrier (ITB), as this reduction in q_e is called, is created by having a reversed safety factor $q(r)$ profile. Owing to their high-speed motion along the field lines, the electrons are the first to find the magnetic field structure has a region of vanishing magnetic shear. From number theory, the reversed profile makes a large gap in the density of the rational surfaces [24]. Such a gap in the density of rational surfaces is immediately reflected in the ETG mode structures and reduces the electron transport. Simple Toy Models of how this change in the spectral distribution of the turbulence and the immediate impact in reducing the electron transport are given in Balescu [25]. The simplicity of the models gives them a universality that may prove to be the best way to verify these models. In essence the standard model for the transition from well-confined orbits to chaotic electron orbits is changed when there is a region of reversed magnetic shear. A new family

of more robust integral surfaces for the electron guiding center orbits is created as the magnetic shear goes through zero. Just before the reversal there can be regimes with extended radial zone of very low magnetic shear that are also known to produce better electron thermal confinement. These regimes known as Optimized Shear (OS) discharges were widely used in the JET tokamak to produce high Q fusion plasmas. Theoretically, these OS discharges have a wider spacing of the rational surfaces than the standard H mode discharges.

CONCLUSION

We show with examples from Tore Supra, NSTX, TCV and FTU how the electron thermal flux from power balance with several RF heating mechanisms is explained by the ETG [small scale electron temperature gradient driven turbulence model]. Earlier similar efforts to explain the anomalous electron fluxes with ion gyro-radius scale models have lead to serious problems with the qualitative inconsistencies between the data and the models. Thus, the ETG model has become the standard model for explaining electron transport in toroidal systems. In the future, the same model at higher plasma beta seems to be working for explaining the transport in the GAMMA-10 tandem mirror where the ITG modes are stabilized by the ion temperature anisotropy and the large value of T_i/T_e. The large T_i/T_e regimes in tokamaks have also indicated that the long wavelength ITG modes are stable yet the electron transport is the typical character explained by the ETG model.

Finally, we summarize that the ETG model produces large transport in the gyrokinetic simulations due to the strong inverse cascade of the quasi-2D nature of the turbulence. The very high density of the rational surfaces at this small millimeter scale of the turbulence and the inverse cascade allow the formation of radially extended convective electric field structures that give a large electron transport that explains much of the mystery of the five decade old problem of the high value and universal character of the electron transport that is called to special attention in Kadomtsev [26]. A full understanding of the problem remains for a future generation of plasma physicists and the ITER experiment's success in reaching the highest fusion Q_f values will certainly be strongly impacted by the value of the electron temperature that can be reached in its discharges. In the large ITER device ($R/a = 6\,\text{m}/2\,\text{m}$) the values of T_e and T_i will be closely coupled with T_e only slightly higher than T_i from the alpha particle fusion products being the dominant plasma heating power for $Q_f > 5$. The anomalous electron temperature transport, thus will be controlled and maintained to acceptable values as determined by integrated predictive code modelings using

the ETG models for the base-line χ_e.

In such a large, complex plasma confinement machine as ITER the plasma system becomes not unlike a weather system in regards to their being many pathways and many feedback loops for the input powers and particle sources to find there wait to divertor chamber and walls of the vessel. Thus, there are exciting opportunities at many levels to contribute to the development of theory and modeling of ITER during the time of its construction and initial operation.

---

[1] K. M. Young, Phys. Fluids **10**, 213 (1967).

[2] L. A. Artsimovich, A. V. Gluchkov, and M. P. Petrov, JETP Lett **11**, 304 (1970).

[3] D. Bohm, E. H. S. Burhop, and H. S. W. Massey, in *The characteristics of electrical discharges in magnetic field*, edited by A. Guthrie and R. K. Wakerling (New York, McGraw-Hill, 1949).

[4] T. Ohkawa, M. Yoshikawa, R. E. Kribel, A. A. Schupp, and T. H. Jensen, Phys. Rev. Lett. **24**, 95 (1970).

[5] D. M. Meade and S. Yoshikawa, Phys. Fluids **10**, 2649 (1967).

[6] G. T. Hoang, C. Bourdelle, X. Garbet, G. Giruzzi, T. Aniel, W. H. M. Ottaviani, and P. Zhu, Phys. Rev. Lett. **87**, 125001 (2001).

[7] T. H. Stix, Nucl. Fusion **15**, 737 (1975).

[8] W. Horton, H. V. Wong, P. J. Morrison, A. Wurm, J. H. Kim, J. C. Perez, J. Pratt, G. T. Hoang, B. P. LeBlanc, and R. Ball, Nuclear Fusion **45** (2005).

[9] V. Basiuk, J. F. Artaud, F. Imbeaux, X. Litaudon, A. Becoulet, L.-G. Eriksson, G. T. Hoang, G. Huysmans, D. Mazon, D. Moreau, et al., Nucl. Fusion **43**, 822 (2003).

[10] A. Jacchia, F. D. Luca, S. Cirant, C. Sozzi, G. Bracco, A. Brushi, P. Buratti, S. Podda, and O. Tudisco, Nucl. Fusion **42**, 1116 (2002).

[11] E. Asp, J.-H. Kim, W. Horton, L. Porte, E. Fable, and O. Sauter, preprint (2007).

[12] G. W. Hammett and F. W. Perkins, Phys. Rev. Lett. **64**, 3019 (1990).

[13] H. Sugama, T. H. Watanabe, and W. Horton, Phys. Fluids **8**, 26172628 (2001).

[14] F. Jenko and W. Dorland, Phys. Rev. Lett. **89**, 225001 (2002).

[15] W. M. Nevins, J. Candy, S. Cowley, T. Dannert, A. Dimits, W. Dorland, C. Estrada-Milla, G. W. Hammett, F. Jenko, M. J. Pueschel, et al., Phys. Plasmas **13**, 122306 (2006).

[16] J. Li and Y. Kishimoto, Phys. Plasmas **9**, 1241 (2002), eTG, slab, gyrofluid.

[17] J. Li and Y. Kishimoto, Phys. Plasmas **11**, 1493 (2004).

[18] C. Holland and P. H. Diamond, Phys. Plasmas **9**, 3857 (2002).

[19] T. H. Watanabe and H. Sugama, Nucl. Fusion **46**, 24 (2006).

[20] S. Kaye, F. Levinton, D. Stutman, K. Tritz, H. Yuh, M. Bell, R. Bell, C. Domier, D. Gates, W. Horton, J. Kim, B.. LeBlanc H. Park, et al., Nucl. Fusion **47**, 499 (2007).

[21] J. W. Connor, C. M. Roach, R. J. Hastie, P. Helander, T. J. Martin, D. J. Applegate, N. Joiner, M. Reshko, S. Saarelma, W. D. Dorland, et al., IAEA Fusion Energy Conference,TH2/P2-2, Chengdu 16-21 October 2006.

[22] X. L. Zou, L. Colas, M. Paume, J. M. Chareau, L. Laurent, P. Devynck, and D. Gresillon, Phys. Rev. Lett. **75**, 1090 (1995).

[23] L. Colas, X. L. Zou, M. Paume, J. M. Chareau, L. Guiziou, G. T. Hoang, Y. Michelot, and D. Gresillon, Nucl. Fusion **38**, 903 (1998).

[24] A. D. Beklemishev and W. Horton, Phys. Plasmas **4**, 200 (1992).

[25] R. Balescu, *Aspects of anomalous transport in plasmas* (Institute of Physics Publishing, 2005), chap. 15, Series in Plasma Physics.

[26] B. B. Kadomtsev, *Tokamak plasma : a complex physical system* (Institute of Physics Pub, 1992).